Check for updates

Advanced Functional Materials

ADVANCED FUNCTIONAL MATERIALS
www.afm-journal.de

RESEARCH ARTICLE OPEN ACCESS

Formation of Quasi-Decoupling Interface on Li-Metal Anodes in High Donor Electrolyte

Hyerim Kim[1] | Sunggun Lim[2] | Shivam Kansara[1] | Jimin Park[1] | Hyoju Lee[2] | Hyokyeong Kang[1] | Soohyung Park[3] | Chihyun Hwang[4] | Hansu Kim[1,2] | Jang-Yeon Hwang[1,2]

[1]Department of Energy Engineering, Hanyang University, Seoul, Republic of Korea | [2]Department of Battery Engineering, Hanyang University, Seoul, Republic of Korea | [3]Advanced Analysis Center, Korea Institute of Science and Technology, Seoul, Republic of Korea | [4]Batteries Research Center Korea Electronics Technology Institute, Seongnam, Gyeonggi, Republic of Korea

Correspondence: Chihyun Hwang (chwang@keti.re.kr) | Hansu Kim (khansu@hanyang.ac.kr) | Jang-Yeon Hwang (jangyeonhw@hanyang.ac.kr)

Received: 9 February 2026 | **Revised:** 3 April 2026 | **Accepted:** 22 April 2026

Keywords: dendrite-free | electrolytes | Li-metal anode | quasi-decoupling additive

ABSTRACT

Li-metal batteries (LMBs) emerge as the "holy grail" of energy storage owing to their high energy density contributed by the Li-metal anode. In this study, lithium ditelluride (Li_2Te_2) is introduced as an electrolyte additive, yielding lithium telluride (Li_2Te) on the Li-metal anode (LMA), establishing a quasi-decoupled interface that reduces electrolyte decomposition. To create an aggressive and high Gutmann donor number environment, dimethyl sulfoxide (DMSO) is employed as a solvent in the electrolyte. Lithium nitrate ($LiNO_3$) is initially used as an additive to protect the LMA surface from DMSO; however, the Li-metal interface modified by $LiNO_3$ cannot block the electron transfer between high donor DMSO and LMA. Owing to its low formation enthalpy (−101.94 kJ mol^{-1}), Li_2Te_2 spontaneously converts to Li_2Te upon contact with Li, effectively blocking electron transfer from DMSO through its large bandgap (E_g = 2.549 eV) and minimal Bader charge transfer (−0.044 |e|). Li_2Te establishes a quasi-decoupled interface that electronically isolates Li from the DMSO. In addition, Li_2Te exhibits strong lithiophilic and Li^+ conductive characteristics, which drive the dendrite-free electrodeposited morphology. Introduction of Li_2Te_2 additive in DMSO-based electrolyte enhances the cycling stability of LMA in half-cells and full-cells, whereas the cells fail without Li_2Te_2.

1 | Introduction

Owing to their high energy density, Li-metal batteries (LMBs), which employ Li-metal as the anode, have attracted attention as promising alternatives to conventional Li-ion batteries, which employ graphite as the anode [1, 2]. Li-metal possesses a high theoretical capacity (3860 mAh g^{-1}) and low redox potential (−3.04 V vs. standard hydrogen electrode) [2–8]. However, the practical realization of LMBs must overcome several obstacles owing to the high reactivity of Li with the electrolyte [9]. For example, continuous parasitic reactions between Li and the electrolyte deplete both the Li-metal anode and electrolyte, resulting in low coulombic efficiency (CE) and poor cycling stability of the Li-metal anode [9]. A non-uniform current distribution on the Li-metal anode causes uneven Li electrodeposition, leading to in the evolution of dead Li and Li dendritic growth during cycling [7]. Continuous Li dendritic growth penetrates separators and generates short-circuits, thereby threatening safety. Therefore, forming a uniform and robust solid electrolyte interface (SEI) is essential to mitigate undesired side reactions in LMBs.

Hyerim Kim and Sunggun Lim contributed equally to this work.

This is an open access article under the terms of the Creative Commons Attribution-NonCommercial-NoDerivs License, which permits use and distribution in any medium, provided the original work is properly cited, the use is non-commercial and no modifications or adaptations are made.
© 2026 The Author(s). *Advanced Functional Materials* published by Wiley-VCH GmbH

For decades, several strategies such as employing host material or artificial SEI and modifying electrolyte solutions have been reported to overcome these problems. In particular, electrolyte modification through a various combination of solvents, salts, and additives is an effective and crucial approach for constructing stable SEIs on Li-metal anodes [1, 6]. However, the SEI can redissolve into the solvent, thereby exposing fresh Li to the electrolyte. This fresh Li exposure promotes further electrolyte decomposition and the formation of an uneven and thick SEI on the Li-metal anode. This issue is particularly severe when electrolytes that contain high donor number (DN) solvents are used. In general, high-DN solvents can dissolve high-donor salts (i.e., $LiNO_3$) that can form conductive and rigid SEI [7, 8]; however, high-DN solvent molecules readily release electrons, making them powerful nucleophiles and therefore bind strongly to Li^+ (strong solvation) and readily decompose on their own when in contact with the Li-metal surface [7, 8]. Therefore, a strategy for quasi-decoupling or decoupling Li from the electrolyte to reduce parasitic reactions is required in electrolyte engineering upon using high-DN solvent.

In this study, a quasi-decoupling strategy for protecting the Li-metal anode from aggressive high-DN solvent was introduced by formulating lithium ditelluride (Li_2Te_2) in the electrolyte of 1 M lithium bis(trifluoromethanesulfonyl)imide (LiTFSI) and 6 wt.% $LiNO_3$ dissolved in dimethyl sulfoxide (DMSO). In the previous literature, it was reported that the introduction of $LiNO_3$ can significantly enhance the mechanical rigidity and improve ionic conductivity of the SEI layer by forming an inorganic Li_3N compound. However, Li_3N has semiconductor features with a small bandgap, which could partially allow electron transport, causing electrolyte decomposition, particularly when using high DN solvents. Li_2Te_2 spontaneously converts to Li_2Te upon contact with Li and forms Li_2Te on the Li-metal anode. The resulting Li_2Te featured acceptor and low charge-transfer properties with DMSO and a relatively wide bandgap (E_g), blocking the path of electrons from DMSO to the Li-metal; namely, this approach can block the direct electronic interaction of electrolytes with Li through a quasi-decoupling effect. Li_2Te also enabled high Li^+ diffusion with strong adsorption and a low Li^+ diffusion barrier. Along with the positive effect of the $LiNO_3$ additive, as a result, galvanostatic tests using symmetrical Li||Li cells with the Li_2Te_2 additive revealed long-term cycling stability at approximately 2300 h at a capacity loading of 2 mAh cm^{-2} and current density of 2 mA cm^{-2}. As a proof-of-concept, the full cell coupling with $LiFePO_4$ (LFP; 2 mAh cm^{-2}) as the cathode further demonstrated potential use of the proposed strategy in Li-metal batteries.

2 | Results and Discussion

DMSO was selected as a solvent for electrolyte engineering due to its strong dissolving ability and creating highly reactive environment attributed to its high DN property (29.0 kcal mol^{-1}); however, DMSO has rarely been applied in LMB systems because of its aggressive chemical reactivity with Li-metal [10]. On the other hand, this property enables the assessment of the degree of reaction suppression in a highly reactive chemical environment. Therefore, in this study, 1 M LiTFSI dissolved in DMSO is used as baseline electrolyte (denoted as B0). SEI modulation from the decoupling strategy, which blocks electron transfer between Li and electrolyte, is crucial to form a stable interface on the Li-metal anode. In the previous studies, $LiNO_3$ has been considered one of the most effective additives to stabilize the Li-metal surface because $LiNO_3$-derivative Li_3N is a distinguished inorganic, ionic-conductive material facilitating Li^+ transport in SEI on Li-metal anode, and such inorganic components are insoluble in electrolytes, enabling the formation of a robust SEI [11, 12]. In that reason, many studies were reported applying high concentrations of $LiNO_3$ with high DN solvents due to their high DN properties [7–9]. However, the high DN solvents are generally unstable with the Li-metal anode, leading to continuous electrolyte decomposition even under a Li_3N-rich SEI environment [13]. Moreover, Li_3N couldn't fully block the electron transfer due to its semiconductor nature with a comparatively small bandgap, which can permit the electron transfer through the material, implying the possibility of irreversible redox reaction [14]. In other words, although $LiNO_3$ commonly form Li_3N on Li-metal anode through spontaneous reaction of "$3Li^+ + N^{3-} \rightarrow Li_3N$" with a low formation energy of $\Delta H_f = -119.84\ kJ\ mol^{-1}$, it is insufficient to prevent the initial SEI dissolution and electrolyte decomposition [15]. Therefore, here, we started electrolyte design using density functional theory (DFT) for SEI modulation utilizing $LiNO_3$ and Li_2Te_2 as additives to form an ionically conductive and quasi-decoupling interphase. Introducing Li_2Te_2 as an additive is an effective approach to initiate the formation of Li_2Te via following reaction: $Li_2Te_2 + 2Li \rightarrow 2Li_2Te$($\Delta H_f = -101.94\ kJ\ mol^{-1}$). This reaction is spontaneously generated, with a low enthalpy energy of −101.94 kJ mol^{-1}. However, Li_3N is thermodynamically more stable than Li_2Te, exhibiting a more negative formation energy of −119.84 kJ mol^{-1} for Li_3N. Accordingly, Li_3N is more likely to form preferentially on the Li-metal anode, may leading to Li_3N-rich inner SEI while Li_2Te could dominate the outer SEI before cycling. A more negative formation enthalpy of Li_3N reflects its higher bulk thermodynamic stability compared to Li_2Te, suggesting a lower intrinsic tendency for bulk decomposition. However, electronic decoupling at the Li–electrolyte interface is governed primarily by electronic structure—such as band-gap magnitude and interfacial charge transfer—rather than bulk thermodynamics. We evaluated charge-density differences (CDDs) at the interfaces to quantify charge redistribution upon contact (Figure 1a–c). The blue vertical box regions shown in Figure 1 highlight the interfacial region between various substrates (Li, Li_3N, and Li_2Te) and a DMSO molecule used for the analysis. The CDD plots revealed less interfacial charge rearrangement for the Li_2Te–DMSO interface than for the Li–DMSO or Li_3N–DMSO (Figure 1a–c) interfaces, indicating a weak electronic interaction between DMSO and Li_2Te. Subsequently, Bader charges were calculated to obtain the net electron transfer (Δq) between the two models. The net interfacial charge transfers were 0.560, 0.018, and −0.004 |e| for Li–DMSO, Li_3N–DMSO, and Li_2Te–DMSO, respectively. In absolute terms, Li_2Te transferred 4.5-fold less charge than that of Li_3N and orders of magnitude less than that of the bare Li surface. These values and the CDD isosurfaces indicate a consistent physical picture, in which the bare Li surface injects a large amount of electronic density into the contacting DMSO, creating the electronic precondition for reductive solvent decomposition. Moreover, Li_3N produces a low net electron transfer consistent with its role as an ionically conductive but electronically and partially permissive SEI component, while Li_2Te shows essentially zero net transfer and negligible interfacial CDD, indicating almost no electron exchange with the solvent.

16163028, 2026, 48, Downloaded from https://advanced.onlinelibrary.wiley.com/doi/10.1002/adfm.75656 by Hanyang University Library, Wiley Online Library on [22/11/2026]. See the Terms and Conditions (https://onlinelibrary.wiley.com/terms-and-conditions) on Wiley Online Library for rules of use; OA articles are governed by the applicable Creative Commons License

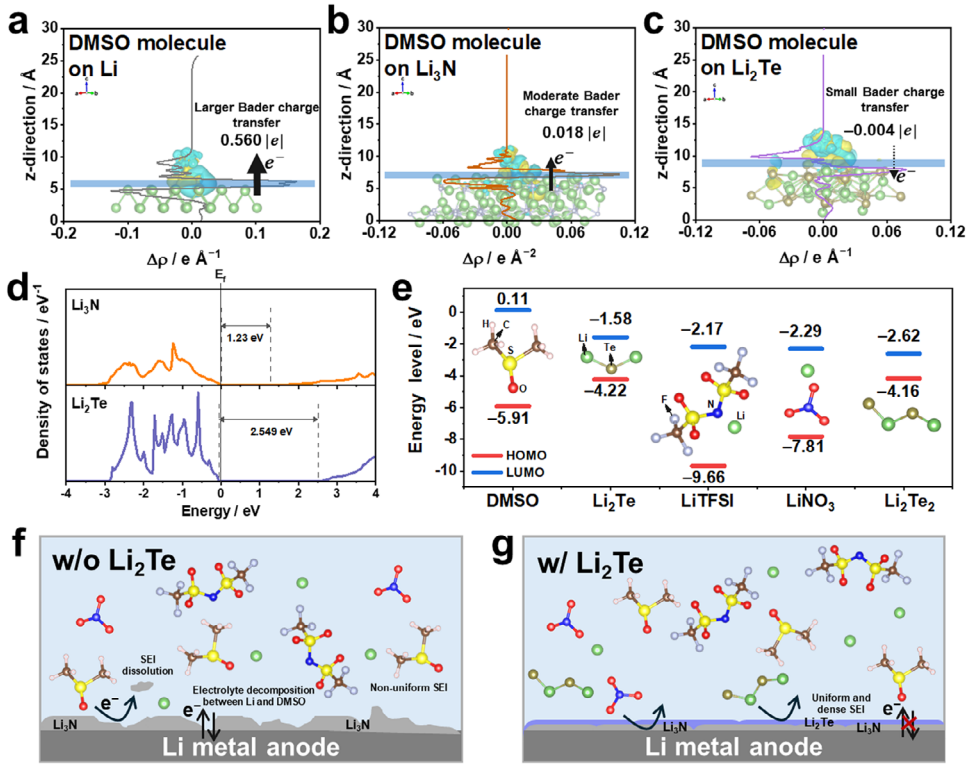


FIGURE 1 | DFT investigation into the effect of Li_2Te on quasi-decoupling from DMSO. CDDs and X-Y plane averages of DMSO on (a) Li, (b) Li_3N, and (c) Li_2Te. (d) Density of states (DOS) for Li_3N and Li_2Te. (e) HOMO and LUMO energy levels of the DMSO solvent, salts, and additives. Schematic illustrations: Potential effects on stabilizing Li-metal anode (f) without and (g) with Li_2Te species.

The near-zero and slightly negative Δq for Li_2Te implies only a tiny polarization of DMSO rather than a true redox event. This results in two important consequences for interfacial chemistry: (i) the electronic driving force for DMSO reduction is removed at Li_2Te-covered sites, and (ii) the low interfacial electron exchange disfavors the dissolution of SEI species into the DMSO medium because the solvent stabilization of charged fragments, which requires significant electron redistribution, is minimal [16]. Surface energies of different Li-based substrates further support the enhanced stability of Li_2Te-containing substrate, which exhibits a lower surface energy in the case of Li_2Te on Li (0.384 J m^{-2}). In contrast, similar surface energies were observed for bare Li (0.554 J m^{-2}) and Li_3N on Li (0.520 J m^{-2}) (Figure S1). These results indicate that the presence of Li_2Te on Li renders the surface thermodynamically more stable, which means less driving force for interfacial reactions with electrolyte [17, 18].

Figure 1d presents the calculated electronic density of states (DOS) of the Li_3N and Li_2Te materials. The DOS of original compounds provides a useful baseline for understanding their intrinsic electronic character and for interpreting how each species behaves when incorporated into an SEI. Two salient points arise from these pristine-material DOS results. First, Li_2Te exhibited a substantially larger bandgap (E_g = 2.549 eV) than Li_3N (E_g = 1.23 eV), suggesting that Li_2Te effectively enables quasi-decoupling between Li and the electrolyte by blocking the electron channel [19, 20]. Second, Li_3N showed appreciable electronic states closer to the Fermi level, whereas Li_2Te had a markedly lower DOS near the Fermi level. These inherent electronic differences indicate that Li_2Te is an intrinsically poorer electronic conductor than Li_3N; therefore, all else equal, Li_2Te is more likely to function as an electronic barrier when present as a thin SEI component. However, the pristine-DOS results set a clear expectation that if Li_2Te preserves its large-gap character at the surface, it will increase the energetic cost of electron transfer into the acceptor orbitals of nearby solvent molecules compared with a Li_3N-like interphase. According to our explicit interfacial calculations, when DMSO is placed on the Li_2Te surface, negligible net Bader charge transfer (Δq = −0.004 |e|) and minimal PDOS overlap between solvent-derived frontier orbitals and Te-derived states are observed. Thus, the intrinsic insulating character of Li_2Te survives at the interface and suppresses the electronic coupling of Li to DMSO [21]. If $LiNO_3$ is preferentially reduced on the Li-metal anode alone, continuous SEI dissolution occurs, facilitating electron transfer to the solvent. All in all, these findings imply that Li_2Te creates a low-energy, electronically inert surface that suppresses electrolyte decomposition more effectively than Li or Li_3N. Thus, forming Li_2Te in the SEI at the initial stage is crucial to stabilize the interface to block side reactions.

The highest occupied molecular orbital (HOMO) and lowest unoccupied molecular orbital (LUMO) energy levels of electrolyte components are useful to predict preferentially reduced chemical species on Li-metal anodes during cycling [14]. HOMO/LUMO levels of DMSO, Li_2Te, LiTFSI, $LiNO_3$, and Li_2Te_2 were calculated using DFT calculations (Figure 1e). Li_2Te_2 exhibited the lowest LUMO energy level, demonstrating its preferential reduction on the Li-metal surface; therefore, the additive Li_2Te_2 provided a rapid route to generate Li_2Te at the Li- metal anode [22]. Namely,

16163028, 2026, 48, Downloaded from https://advanced.onlinelibrary.wiley.com/doi/10.1002/adfm.75656 by Hanyang University Library, Wiley Online Library on [22/11/2026]. See the Terms and Conditions (https://onlinelibrary.wiley.com/terms-and-conditions) on Wiley Online Library for rules of use; OA articles are governed by the applicable Creative Commons License

thermodynamically, Li_2Te_2 is the preferred electron acceptor in the early stages of cycling. In particular, electrons supplied by Li-metal reduced Li_2Te_2 more readily compared with LiTFSI, $LiNO_3$, or DMSO. Li_2Te—the putative SEI product—had the second-highest LUMO energies of the electrolyte-derived species, indicating that once Li_2Te formed, it was comparatively difficult to reduce further. Potential effects on stabilizing the Li-metal anode without and with Li_2Te species are illustrated in Figure 1f,g, respectively. Without Li_2Te, the electrolyte comprising LiTFSI, $LiNO_3$, and DMSO formed unstable and non-uniform SEIs on the Li-metal anode owing to the soluble chemical composition of the SEI and continuous decomposition between Li and DMSO. In contrast, the production of Li_2Te from the Li_2Te_2 additive resulted in a uniform SEI that was not soluble in the electrolyte, thereby blocking electrolyte decomposition (Figure 1g).

$LiNO_3$ is a well-known additive that forms stable, ionically conductive, and robust chemical components, such as Li_3N, Li_2O, and LiN_xO_y, in the SEI layer and effectively suppresses Li dendrite growth, enabling granular-shaped Li deposits [7]. Before fabricating the Li_2Te_2 containing electrolyte, the concentration of $LiNO_3$ was optimized based on 1 M LiTFSI dissolved in DMSO (B0) to determine its synergistic effect with the Li_2Te_2 additive. Various concentrations of $LiNO_3$ (3, 6, and 9 wt.%) were added to B0 (denoted as B3, B6, and B9, respectively), and the physicochemical properties (density, viscosity, and ionic conductivity) of these electrolytes were measured (Figure S2 and Equation 2). The relationship between viscosity and ionic conductivity is explained by the Stokes–Einstein equation followed: [23]

$$D_0 = \frac{k_B T}{6\pi\eta r} \quad (1)$$

where D_0, k_B, T, η, and r represent the diffusion coefficient, Boltzmann constant, temperature, viscosity of the fluid medium, and radius of the solvation shell, respectively. An increasing η leads to a decrease in D_0, which consequently affects the ionic conductivity. With increasing $LiNO_3$ concentration, the density linearly increased while the viscosity and ionic conductivity dramatically increased and decreased, respectively. Higher viscosity (η) results in low D_0, leading to low ionic conductivity, which causes high polarization and accelerates cell degradation due to sluggish Li^+ transport kinetics. The galvanostatic tests of the Li||Li symmetrical cell containing B9 indicated an increased polarization compared with those containing B6, which was consistent with the lower ionic conductivity of B9 (Figure S3). In contrast, the B3 indicated larger polarization due to high reactivity between DMSO and Li, which leads to oxidation of the lithium metal interface and accelerates the decomposition of the electrolyte through chemical and electrochemical reactions, which in turn damages the interfacial layer and hinders the formation of a stable SEI layer [24]. Thus, 6 wt.% $LiNO_3$ was adopted as the optimal concentration to amplify its synergistic effect with Li_2Te_2 in subsequent optimizations.

Li_2Te_2 was simply produced by introducing Li_2Te and Te at a molar ratio of 1:1 in DMSO. To fabricate the electrolyte, Li_2Te and Te were incorporated into the B6 electrolyte, as shown in Figure 2a. Various concentrations of Li_2Te_2 in the electrolyte were also fabricated, as shown in Figure S4. After several days, no precipitation was observed when using 0.05 and 0.03 M Li_2Te_2, suggesting that all the components were completely dissolved in DMSO and Li_2Te_2 was produced (Figure S4b,c). Conversely, using 0.1 M Li_2Te_2 (B6–0.1Li_2Te_2) resulted in the production of insoluble compounds (Figure S4a). Electrochemical evaluation of electrolyte containing the 0.05 and 0.03 M Li_2Te_2 in Li||Li symmetric cells identified 0.05 M as optimal concentration, denoted B6–Li_2Te_2 (Figure S5). To evaluate whether the addition of Li_2Te_2 increases the viscosity of B6, the ionic conductivity was further measured (Figure S6). The negligible difference between B6 and B6–Li_2Te_2 indicates that Li_2Te_2 does not significantly impair ionic conductivity or electrochemical performance. Notably, Li_2Te_2 was fabricated exclusively in the DMSO-based system, which exhibited higher DN, while the use of N-Methyl-2-Pyrrolidone (NMP) (high DN) and polycarbonate (PC) (high dielectric constant) exhibited precipitation of powder (Figure S7) [25]. The prepared B6–Li_2Te_2 was investigated using Ultraviolet–Visible (UV–vis) and Raman spectroscopies to confirm the fabrication of Li_2Te_2 (Figure 2b,c). As shown in the UV–vis spectrum, the B6–Li_2Te_2 electrolyte exhibited absorption peaks at 261 and 335 nm [26]. The presence of Li_2Te_2 was further observed in the Raman spectra of B6, B6–Li_2Te_2, and the DMSO solvent in the range of 120–240 cm^{-1}. Only B6–Li_2Te_2 presented two peaks attributed to Li_2Te_2 [27]. The Li_2Te solution was also investigated to ensure the fabrication of Li_2Te_2 in the B6–Li_2Te_2 electrolyte (Figure S8). The color of 0.05 M Li_2Te or Li_2Te_2 in DMSO was observed after dropping the solution onto glass, and different colors implied different components were produced in the DMSO-based solution. Conversely, the Raman spectrum of Li_2Te in the same range exhibited different peaks, suggesting that the Raman peaks of B6–Li_2Te_2 strongly supported the existence of Li_2Te_2 [28].

The effect of blocking electron transfer by Li_2Te in B6–Li_2Te_2 was experimentally verified by the chronoamperometry test (CA) in Li||Li symmetric cells using B0, B6, and B6–Li_2Te_2 imposing a constant voltage of −10 mV (Figure 2d). Chronoamperometry is a useful technique for predicting electrode reactions, as it involves applying a constant potential to the working electrode and monitoring the resulting current from faradaic processes as a function of time. Among the three samples, B0 exhibited the highest current response, followed by B6, while B6–Li_2Te_2 showed the lowest current response. The current response in the CA test clearly showed that the formation of Li_2Te on the Li-metal surface can significantly suppress electron flow between the electrolyte and the Li-metal surface through the faradaic process. The surfaces of the Li-metal anodes were examined after 60 h to explore the phenomenon observed under the open circuit voltage (OCV) using Time-of-Flight Secondary Mass Spectrometry (TOF-SIMS) (Figure 2e; Figure S9). The Li^-, C^-, F^-, Te^-, and O^- ion fragments of the different electrolytes were compared using 3D rendering maps to infer the reaction (Figure 2e; Figure S10). The C^- and F^- fragments were likely the representative organic and inorganic products of chemical reactions between Li and the electrolytes, respectively. The distributions of C^- and F^- in B0 were dispersed throughout the 3D model, implying that continuous chemical reactions were generated over time. However, those in B6 were concentrated at the surface of Li. Notably, B6–Li_2Te_2 clearly reduced the dispersions of C^- and F^- in the 3D maps, suggesting that fewer chemical reactions compared with B0 and B6 occurred during the same period. In

16163028, 2026, 48, Downloaded from https://advanced.onlinelibrary.wiley.com/doi/10.1002/adfm.75656 by Hanyang University Library, Wiley Online Library on [22/11/2026]. See the Terms and Conditions (https://onlinelibrary.wiley.com/terms-and-conditions) on Wiley Online Library for rules of use; OA articles are governed by the applicable Creative Commons License

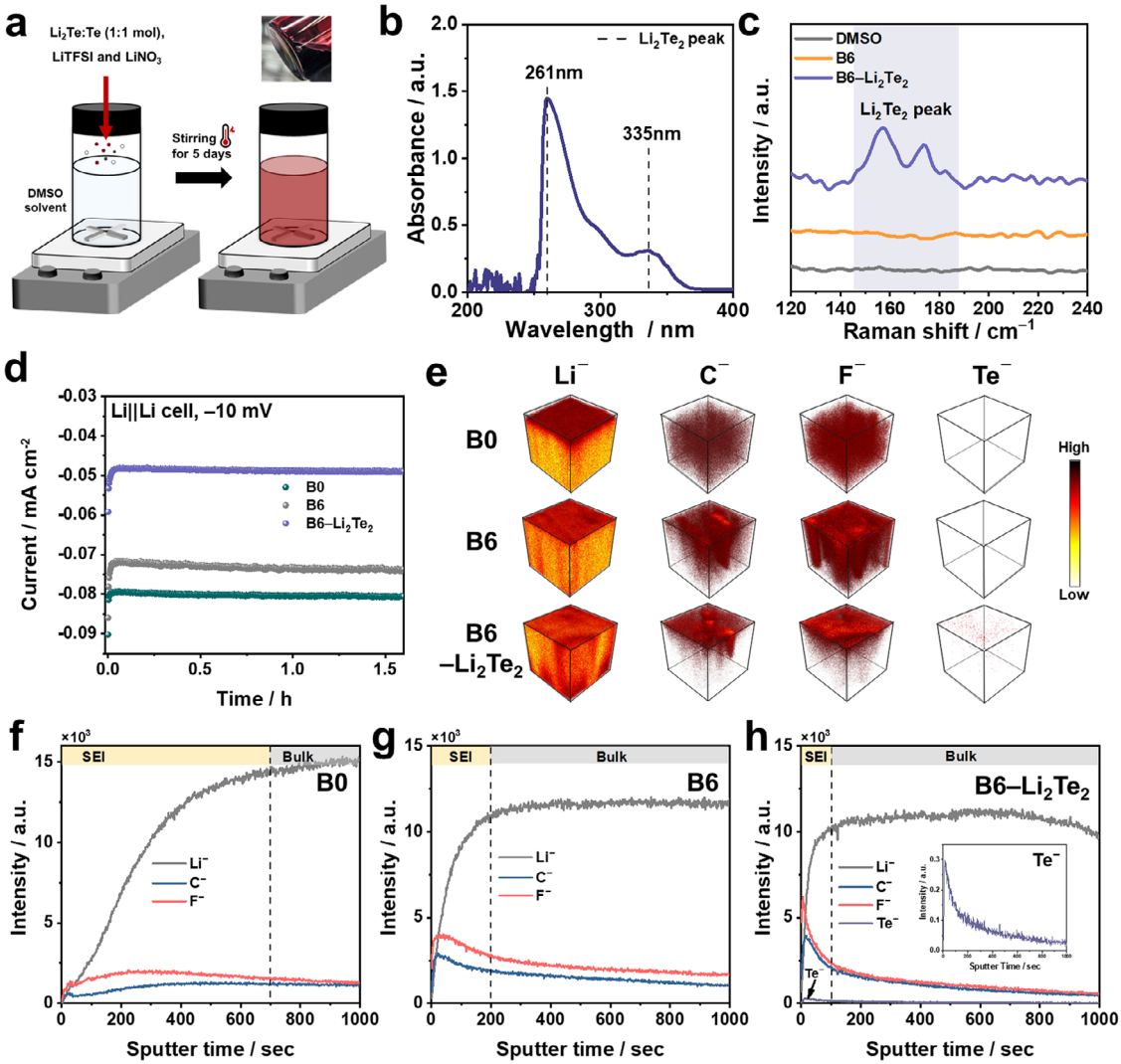


FIGURE 2 | Fabrication of Li_2Te_2 in the electrolyte and production of Li_2Te_2 via the spontaneous reaction between Li and Li_2Te_2. (a) Schematic of Li_2Te_2 fabrication in the electrolyte (B6–Li_2Te_2). Characterization of the fabricated Li_2Te_2 in B6–Li_2Te_2 using (b) UV–vis and (c) Raman spectroscopy at 120–240 cm^{-1}. (d) CA of Li||Li symmetric cell at an overpotential of −10 mV using different electrolytes. (e) 3D-rendered images by TOF-SIMS analysis of the disassembled Li-metal anode from Li||Cu cell under the OCV state after 60 h using different electrolytes. Depth profiling of each Li-metal anode in (e) for investigating initial SEI thickness corresponding to (f) B0, (g) B6, and (h) B6–Li_2Te_2.

addition, Li_2Te existed on the Li surface as fragments of Te^- in B6–Li_2Te_2. From the depth profile of Li^- fragment, it can be supposed that the thickness of the SEI layer [29]. Namely, the prominent different depth of the Li^- fragment of the different electrolytes revealed that B6–Li_2Te_2 possesses a relatively thin SEI layer with respect to B0 and B6 (Figure 2f–h), which is well corresponded to the 3D maps of C^- and F^- fragments [30]. The DFT calculations (Figure 1e) revealed that Li_2Te_2 exhibited the lowest LUMO energy among the species considered; thus, Li_2Te_2 was preferentially reduced at the Li surface during initial cycling. The Te 3d X-ray photoelectron spectroscopy (XPS) results confirmed the formation of Li_2Te in B6–Li_2Te_2 after the first cycle at 2.0 mAh cm^{-2} and 0.2 mA cm^{-2}, with binding energies of nearly 580.8 and 570.5 eV assigned to Te $3d_{3/2}$ and Te $3d_{5/2}$, respectively [31]. Conversely, no peak evolutions were observed for B0 and B6 (Figure S10). Therefore, Li_2Te_2 both chemically and electrochemically reacted with Li to form Li_2Te on the anode surface.

The chemical compositions of the SEI layer on the Li-metal anode in different electrolytes were characterized using XPS and TOF-SIMS. The samples were collected after the initial five cycles in symmetric Li||Li cells (stripping) at a capacity loading of 0.5 mAh cm^{-2} and current density of 0.5 mA cm^{-2}. The Li 1s, C 1s, N 1s, and Te 3d XPS spectra of the SEI layers formed in the B0, B6, and B6–Li_2Te_2 electrolyte are shown in Figure 3a. Note that in this study, XPS spectrum data can only discuss the qualitative comparison between the samples. The peaks at 54.8, 55, 55.2, 55.6, and 56 eV observed in the Li 1s XPS spectrum corresponded to Li^0, Li_2CO_3, Li_3N, Li_2O, and LiF, respectively [32–36]. From the intensity of the Li^0, it can be supposed that the thickness of the SEI layer (i.e., decomposition level of the electrolyte solution). Namely, prominent differences in the Li^0 metallic peaks of the different electrolytes revealed that B6–Li_2Te_2 possesses a relatively thin SEI layer with respect to B0 and B6 [37]. The inorganic SEI components, such as Li_2CO_3, Li_3N, Li_2O, and LiF, could be formed by the decomposition of

16163028, 2026, 48, Downloaded from https://advanced.onlinelibrary.wiley.com/doi/10.1002/adfm.75656 by Hanyang University Library, Wiley Online Library on [22/11/2026]. See the Terms and Conditions (https://onlinelibrary.wiley.com/terms-and-conditions) on Wiley Online Library for rules of use; OA articles are governed by the applicable Creative Commons License

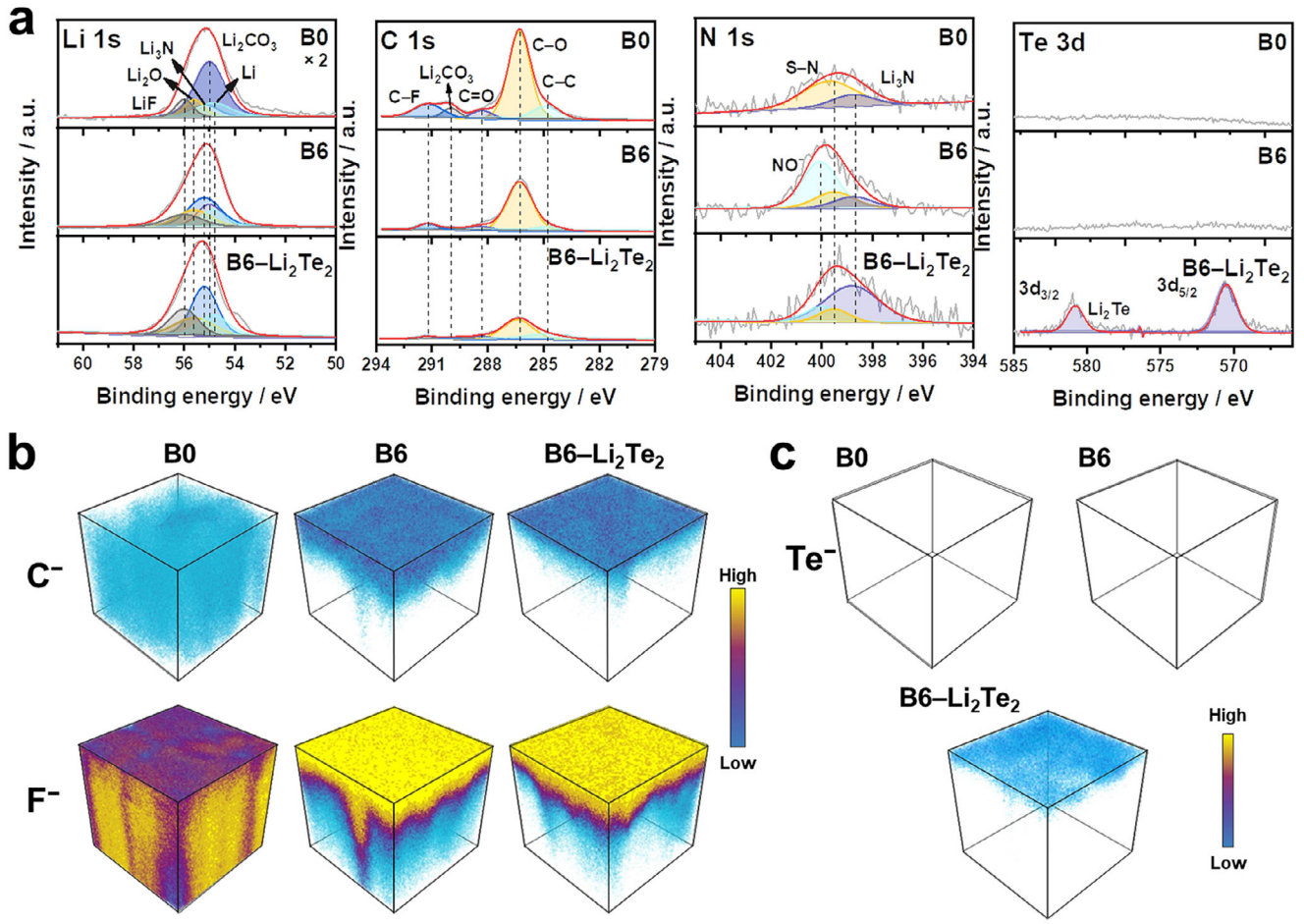


FIGURE 3 | Characterizations of the SEI layer on the Li-metal anode using different electrolytes after five cycles at a capacity loading and current density of 0.5 mAh cm^{-2} and 0.5 mA cm^{-2}, respectively. XPS spectra of the (a) Li 1s, C 1s, N 1s, and Te 3d regions of the SEI layer. 3D rendering of the TOF-SIMS results of the SEI layer with (b) C^-, F^-, and (c) Te^- fragments.

the electrolytes. In particular, Li_2CO_3 is considered to originate from the decomposition of the organic solvent (DMSO), whereas Li_3N, Li_2O, and LiF mainly originate from salt decomposition (LiTFSI or $LiNO_3$). For example, Li_2CO_3 and LiF contribute to the formation of a mechanically robust SEI that can sustain without the dissolution in organic solvent while having a poor ionic conductivity [38–40]. On the other hand, Li_3N and Li_2O have provided good ionic diffusion in the SEI layer. The signals related to electrolyte decomposition from solvent molecules were generally observed in the C 1s spectrum [41]. The peaks at 284.8, 286.4, 288.4, 289.8, and 291.2 eV in the C 1s spectrum were attributed to C—C, C—O, C═O, Li_2CO_3, and C—F bonding, respectively [42, 43]. By introducing $LiNO_3$ and Li_2Te_2 additives, the relative intensities of the peaks in C 1s spectra are reduced, revealing that electrolyte decomposition, likely DMSO solvent, was suppressed. In particular, Li_2CO_3 mostly disappeared in the Li 1s and C 1s spectrum of B6–Li_2Te_2, implying that electrolyte decomposition was inhibited by Li_2Te. The N 1s spectrum showed deconvoluted peaks at 398.8, 399.5, and 399.9 eV, indicating Li_3N, S—N, and NO^- bonding, respectively [9, 44]. These N 1s peaks in B0 were attributed to LiTFSI decomposition. From B6 to B6–Li_2Te_2, the NO^- bond was decreased, and the dominant Li_3N portion was observed. This is because the presence of Li_2Te in SEI can inhibit the charge-transfer between DMSO and Li-metal, rather facilitating the spontaneous reaction between Li-metal and NO_3^- then. Owing to its low formation enthalpy (−101.94 kJ mol^{-1}), Li_2Te_2 spontaneously converts to Li_2Te upon contact with Li (Figure 2e; Figure S10). In addition, as shown in Figure 1e, Li_2Te_2, with the lowest LUMO energy level compared to other components, can be preferentially reduced on the Li-metal anode during cycling, forming Li_2Te. Notably, the Te 3d spectrum of B6–Li_2Te_2 in Figure 3a exhibited the only Li_2Te signal compared to that in Figure S10, implying that Li_2Te_2 was fully reduced to Li_2Te during cycling. Depth profiling of the N 1s and Te 3d spectra was further performed to identify the dominant components in the inner and outer SEI layer (Figure S11). In agreement with the trend expected from the formation enthalpies, the Li_3N signal increased, and Li_2Te decreased with increasing etching time, indicating a Li_3N-rich inner SEI and a Li_2Te-rich outer SEI layers.

To better understand the formation of the different SEI in different electrolytes, TOF-SIMS of the Li-metal surface was used to visualize the distribution of chemical species in the SEI layer after cycling (Figure 3b,c). The ion fragments of C^- were designated as organic species, suggesting solvent decomposition on the Li-metal anode [45]. The 3D-rendered box confirmed that the degree of C^- fragments was gradually decreased from B0 to B6 and then B6–Li_2Te_2, suggesting that Li_2Te in SEI effectively inhibited the parasitic solvent decomposition by helping the $LiNO_3$. The 3D-rendered box of F^- exhibited a strong signal of F^- on the

16163028, 2026, 48, Downloaded from https://advanced.onlinelibrary.wiley.com/doi/10.1002/adfm.75656 by Hanyang University Library, Wiley Online Library on [22/11/2026]. See the Terms and Conditions (https://onlinelibrary.wiley.com/terms-and-conditions) on Wiley Online Library for rules of use; OA articles are governed by the applicable Creative Commons License

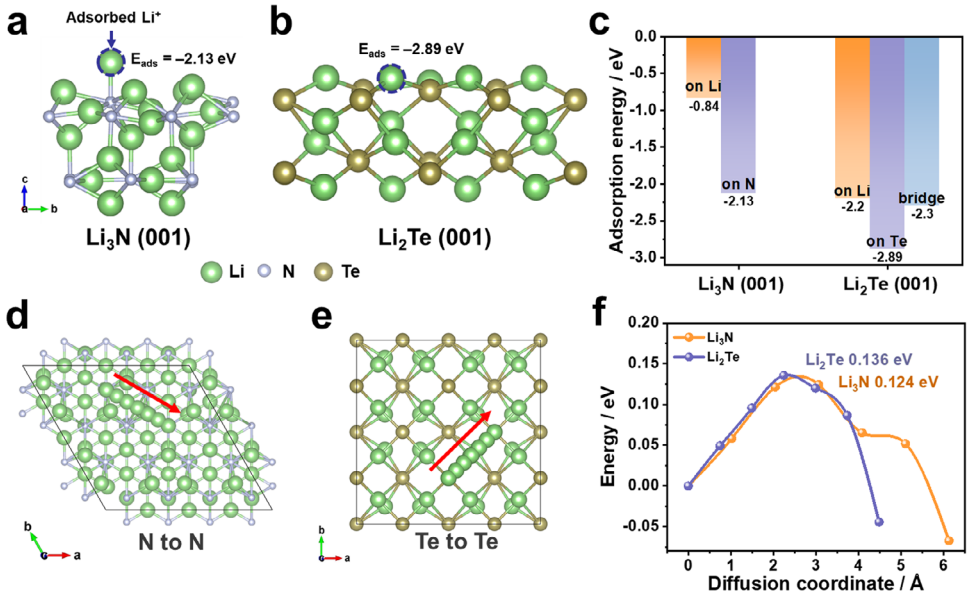


FIGURE 4 | Adsorption model structures of (a) Li_3N and (b) Li_2Te. (c) Various adsorption energy values at different sites in Li_3N (on Li and N) and Li_2Te (on Li, Te, and bridge). Optimized diffusion pathways of Li using NEB calculations through (d) N to N on Li_3N and (e) Te to Te on Li_2Te. (f) NEB calculation of the Li^+ diffusion barrier on Li_3N and Li_2Te corresponding to (d,e).

surface of Li in B6 and B6–Li_2Te_2, indicating inorganic-rich SEI including fluorinated species. Notably, B6–Li_2Te_2 readily weakens the intensity of both C^- and F^- signal with increasing sputtering time compared to B0 and B6, implying a relatively thin SEI layer [45, 46]. The ion fragments of Te^- only generated in B6–Li_2Te_2, and it showed a clear signal after cycling compared to the OCV state in Figure 2f. The Te^- signal remained uniformly distributed over the Li-metal surface after further cycling, indicating that the Li_2Te continued to provide sufficient coverage to quasi-decouple Li-metal from the electrolyte (Figure S12). As observed in the CDD results (Figure 1a–c), Li_2Te as a quasi-decoupling component showed a minimal charge transfer with DMSO, which can reduce the electron supply from Li to DMSO and suppress electrolyte decomposition. Therefore, this characteristic resulted in a thinner, more uniform, and more inorganic SEI when using B6–Li_2Te_2 compared to using B0 and B6, as evidenced by XPS and TOF-SIMS.

To verify the lithiophilic and ionically conductive characteristics of SEI upon using $LiNO_3$ and Li_2Te_2 additives, the Li-adsorption energies and migration barriers were calculated for Li_3N and Li_2Te using DFT (Figure 4). First, the adsorption energy quantifies the lithiophilicity of a substrate by measuring how strongly Li binds to different surface sites. The most stable adsorption energies were −2.13 eV on Li_3N and −2.89 eV on Li_2Te (Figure 4a,b), indicating that Li_2Te binds Li more strongly than does Li_3N; therefore, Li_2Te can function as a preferred lithophilic nucleation/anchoring site that promotes uniform Li deposition [47]. The additional adsorption sites of Li_3N and Li_2Te are presented in Figure 4c. Every site of Li_2Te (on Li, Te, and bridge) strongly adsorbed Li compared with that of Li_3N (on Li and N). The distinction between thermodynamic driving force and reaction kinetics should be emphasized regarding these results. Although $\Delta H < 0$ indicates that the conversion to Li_2Te is energetically favored, the rate of conversion depends on the activation barrier for the relevant chemical or electrochemical pathway. To quantify the kinetic ability of the Li_3N- and Li_2Te-containing SEI in supporting Li^+ transport, representative migration barriers were computed along optimized in-plane diffusion pathways using the climbing-image nudged elastic band (CI-NEB) method (Figure 4f; Figure S13). Two characteristic hops were identified for each material. For example, Li_3N showed barriers of 0.124 and 0.540 eV, while Li_2Te showed barriers of 0.136 and 0.479 eV. Using a simple random-walk estimate, these barriers translated to order-of-magnitude diffusivities that showed the same trend: both materials supported extremely rapid local ionic motion. However, macroscopic transport was controlled by the largest barrier along the percolation path. The maximum barrier for Li_2Te (0.479 eV) was slightly lower than that for Li_3N (0.540 eV). Consequently, Li_2Te combined strong lithiophilicity with sufficiently low activation energies for long-range Li^+ migration, rendering it at least comparable to (and in some respects superior to) Li_3N as an ionically conductive SEI component. These computed kinetics rationalize the experimentally observed low interfacial resistance, low polarization during plating/stripping, and the formation of stable Li deposits when Li_2Te_2 is used as an additive.

To investigate the effect of SEI layer modified by adding $LiNO_3$ and/or Li_2Te_2 additives on electrodeposition morphology of Li after plating, the morphology change of Li-metal surface was observed using SEM analysis after the electrodeposition of Li in different electrolytes at a capacity loading and current density of 2 mAh cm^{-2} and 0.2 mA cm^{-2} (Figure 5a–c). It should be noted that the chemical instability (high reactivity) between DMSO and Li can procure the pitting corrosion and a faded surface on the Li metal anode surface (see SEM image in Figure S14) [48]. These features can create height variations on the Li metal surface, promoting preferential Li deposition at protruding regions following the tip-growth mechanism, potentially leading to dendrite formation [49]. In addition, high donor DMSO solvent can also dissolve the SEI layer. The damaged SEI can expose fresh Li metal, which accelerates the formation of thick SEI layers through the extent of

16163028, 2026, 48, Downloaded from https://advanced.onlinelibrary.wiley.com/doi/10.1002/adfm.75656 by Hanyang University Library, Wiley Online Library on [22/11/2026]. See the Terms and Conditions (https://onlinelibrary.wiley.com/terms-and-conditions) on Wiley Online Library for rules of use; OA articles are governed by the applicable Creative Commons License

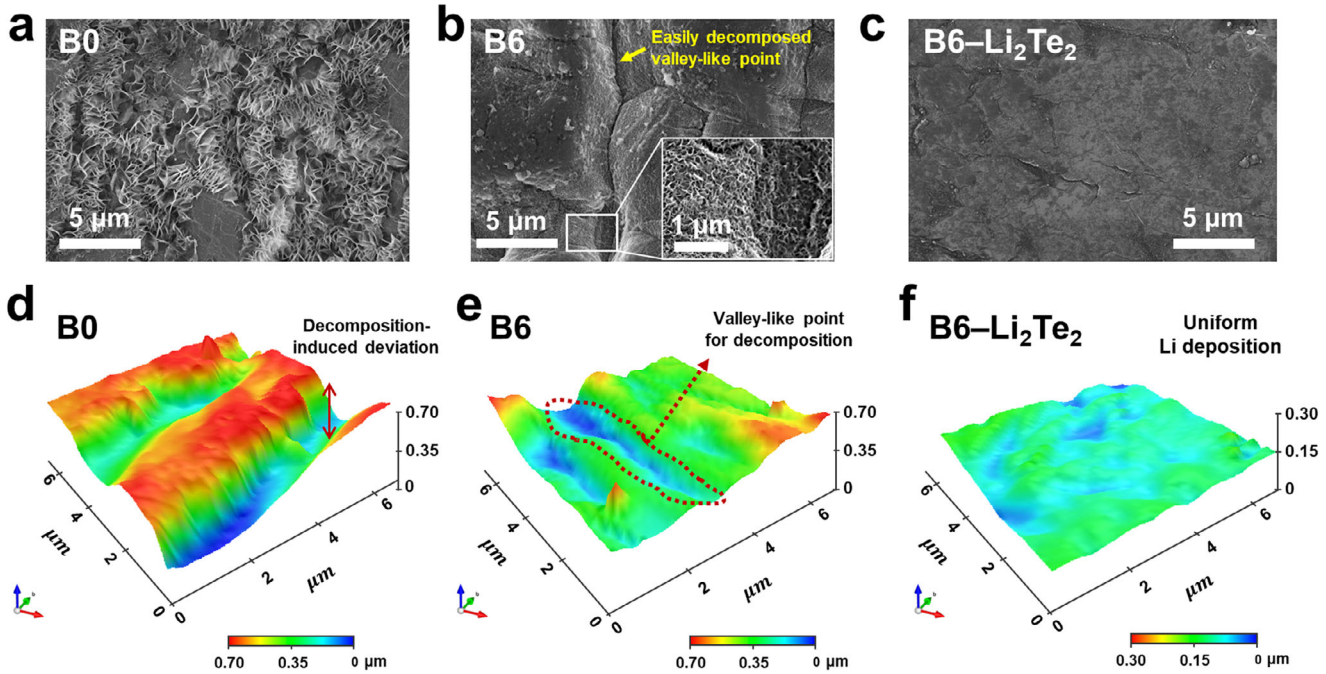


FIGURE 5 | Morphology of the Li-metal surface following electrodeposition at a capacity loading of 2 mAh cm^{-2} and current density of 0.2 mA cm^{-2} in B0, B6, and B6–Li_2Te_2. SEM images of the Li-metal surface using (a) B0, (b) B6, and (c) B6–Li_2Te_2. AFM topographic analyses (6.7 × 6.7 μm scan size) of the 3D height profiles of (d) B0, (e) B6, and (f) B6–Li_2Te_2.

electrolyte reduction (see XPS results in Figure 3a; Figure S15). As a result, eventually, the Li-metal anode using B0 exhibited needle-like Li deposit morphologies with a deep valley (Figure 5a). After adding 6 wt.% $LiNO_3$ (B6), the surface of Li appeared relatively smoother morphology than the B0 sample; however, valley-like regions were still remained and the magnified view revealed needle-like Li deposit morphology similar to the B0 sample. These results indicated that the SEI layer modified by $LiNO_3$ additive was insufficient to suppress aggressive reactions between the Li-metal and DMSO. In contrast, B6–Li_2Te_2 displayed distinct, dense, and smooth surface morphologies of Li-metal anode, indicating that the presence of Li_2Te in SEI layer effectively enhanced the interfacial stability due to lithiophilic interface, good Li^+ diffusion kinetics, and quasi-decoupling between Li and the electrolyte by blocking the electron channel. These morphological differences were more clearly observed in low-magnification SEM images (Figure S16). The 3D-topographic images using atomic force microscopy (AFM) strengthened these results (Figure 5d–f). They revealed a higher deviation for B0 and B6 after plating, indicating a non-uniform plating morphology, while B6–Li_2Te_2 revealed a flat and smooth surface without height fluctuation, consistent with Figure 5c. The height deviations of different electrolytes were compared at the same position, and marked with black dot lines in Figure S17; B0 and B6 exhibited severe fluctuating height profiles (Figure S18). Conversely, B6–Li_2Te_2 exhibited a small deviation and a flat surface.

The average CE was estimated using the Li||Cu symmetric cell to assess the reversibility of Li depending on the electrolyte used (Figure 6a). Using the protocol suggested by Zhang et al., the effect from Cu foil was eliminated, and the accuracy of the results was ensured [50]. After 20 cycles at a capacity loading of 0.5 mAh cm^{-2} and a current density of 0.5 mA cm^{-2}, residual Li on the Cu foil was stripped at a cut-off voltage of 1 V, and the charged capacity (Q_S) was calculated. The CEs were calculated using Equation 3. B0 exhibited a short-circuit after three cycles, and the CE could not be calculated during cycling owing to instability and side reactions at the SEI layer on the Li-metal anode. B6 delivered a lower CE of 89.76% while B6–Li_2Te_2 delivered a high Q_S and high CE of 94.08% owing to the aiding effect of the SEI layer by Li_2Te along with the presence of Li_3N. The initial state of average CE measurement (marked as an asterisk in Figure 6a) was used to confirm the nucleation overpotential of Li deposition (Figure 6b). Nucleation overpotential is used as an indicator of the energy required to form Li nuclei during the first deposition process [51]. The nucleation overpotential was 26 mV for B6–Li_2Te_2 and 79 mV for B6, which is three-fold higher than that for B6–Li_2Te_2. Following Equation S2, the Li particle sizes decreased with increased overpotential [52]. Thus, the initial formation of Li_2Te drives the uniform and particle like nucleation rather than dendritic growth of Li. The effect of Li_2Te in the SEI layer on stability of Li was further confirmed via galvanostatic cycling testing using the Li||Li symmetric cell at a capacity loading and current density of 2 mAh cm^{-2} and 2 mA cm^{-2}, respectively (Figure 6c; Figure S19). The cell with B0 was short-circuited at the early stage of cycling (Figure S19), and the cell with B6 sustained a stable operation for only 50 h. In contrast, the symmetric cell with B6–Li_2Te_2 delivered outstanding cycling stability over 2300 h. On the other hand, the optimized molar concentration of Li_2Te_2 contributing to the formation of Li_2Te was inspected. Furthermore, the cell with B6–Li_2Te_2 maintained stable voltage profiles over 1600 h at a higher capacity loading and current density of 4 mAh cm^{-2} and 4 mA cm^{-2}, respectively (Figure S20). Namely, this approach can form an ionically conductive and chemically stable SEI on the Li-metal surface and thus can operate under high-capacity loading and current density conditions

16163028, 2026, 48, Downloaded from https://advanced.onlinelibrary.wiley.com/doi/10.1002/adfm.75656 by Hanyang University Library, Wiley Online Library on [22/11/2026]. See the Terms and Conditions (https://onlinelibrary.wiley.com/terms-and-conditions) on Wiley Online Library for rules of use; OA articles are governed by the applicable Creative Commons License

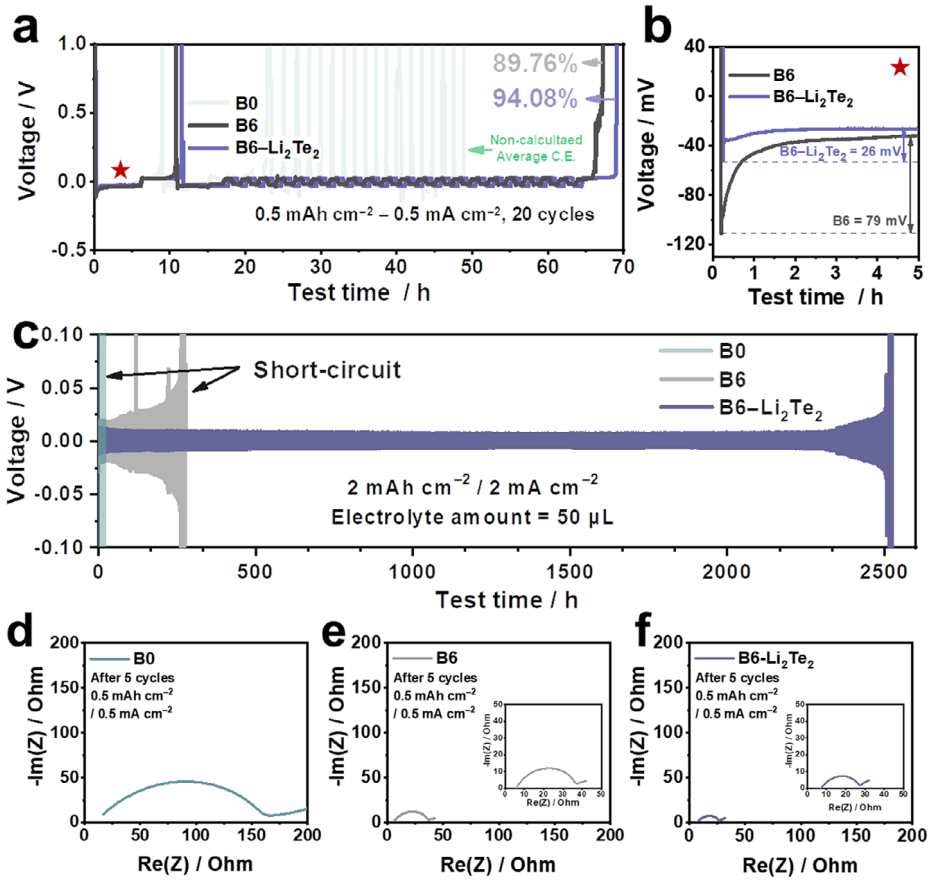


FIGURE 6 | (a) Voltage–time profiles for the CE tests of the Li||Cu asymmetric cell in B0, B6, and B6–Li_2Te_2 used to evaluate Li plating/stripping reversibility. (b) Nucleation potential of the electrodeposited Li in B6 and B6–Li_2Te_2 at a current density of 0.5 mA cm^{-2} marked with a red asterisk in (a). (c) Galvanostatic electrochemical tests of the Li||Li symmetric cells at a capacity loading and current density of 2 mAh cm^{-2} and 2 mA cm^{-2} in different electrolytes. Electrochemical impedance spectra of the Li||Li symmetric cells using (d) B0, (e) B6, and (f) B6–Li_2Te_2 after five cycles at a capacity loading and current density of 0.5 mAh cm^{-2} and 0.5 mA cm^{-2}, respectively.

without significant electrolyte decomposition. The interfacial resistances of the cycled Li||Li symmetrical cells using different electrolytes were evaluated with different SEI compositions using electrochemical impedance spectroscopy (EIS) measurements after five cycles at a capacity loading and current density of 0.5 mAh cm^{-2} and 0.5 mA cm^{-2}, respectively (Figure 6d–f). The EIS spectrum was fitted using the equivalent circuit shown in Figure S21 and the results are provided in Table S1 [53]. The results offer information related to the interface of the Li-metal anode depending on the transfer kinetics of Li^+ [54, 55]. The cell with B0 exhibited a larger resistance, indicating that the severe side reaction between Li-metal and the DMSO solvent resulted in an unstable interphase and damage to the Li surface. Moreover, the cells using B6 and B6–Li_2Te_2 exhibited lower resistances compared with those using B0. Particularly, the B6–Li_2Te_2 electrolyte showed a lower resistance compared with the B0 and B6 electrolytes (Figure 6d,e). The formation of a highly stable SEI layer, including Li_3N and Li_2Te, facilitated Li^+ diffusion and inhibited side reactions between the Li-metal and DMSO solvent, resulting in a reduced interphase resistance.

The practical feasibility of using B6–Li_2Te_2 as an electrolyte was further evaluated at an areal capacity of 2 mAh cm^{-2} for the LFP cathode in the voltage range of 2.5–3.9 V under 0.1 C (0.2 mA cm^{-2}). The full cell with the B0 electrolyte did not reach 3.9 V and showed continuous irreversible capacity evolution, suggesting that an uncontrollable parasitic reaction between Li- metal and DMSO occurred during the charging process (Li plating process for Li-metal anode) (Figure 7a). Figure S22 depicted the charge–discharge voltage profiles of B6 and B6–Li_2Te_2 at 0.1 C. The cells performed well with a high reversible capacity of 137.5 mAh g^{-1} even if only $LiNO_3$ was added in addition to Li_2Te_2 into the electrolyte, indicating that the $LiNO_3$ additive can initially protect the Li-metal surface from serious DMSO solvent decomposition. In a cycling test at 1 C, however, the capacity of the cell using B6 exhibited a continuous and rapid capacity fading, and eventually, it experienced the continuous irreversible capacity evolution similar to the cell using the B0 electrolyte (Figure 7b); this means that the protective layer induced by the $LiNO_3$ additive is not enough to endure the aggressive chemical reaction between Li-metal and DMSO. On the other hand, the cell using B6–Li_2Te_2 delivered a reversible capacity of 120 mAh g^{-1} and exhibited a stable cycle performance of 99.75% after 40 cycles at 1 C (Figure 7c). Figure 7d compared the cycling performances of the full cells using B6 and B6–Li_2Te_2. To better understand the effect of Li_2Te_2 additive on cycling stability, the full cells using B6 and B6–Li_2Te_2 were disassembled after the seventh cycle in the discharge state (after stripping process for Li-metal anode) and then investigated the surface morphology of the Li-metal anode and crystal structure of the LFP cathode (Figure 7e,f).

16163028, 2026, 48, Downloaded from https://advanced.onlinelibrary.wiley.com/doi/10.1002/adfm.75656 by Hanyang University Library, Wiley Online Library on [22/11/2026]. See the Terms and Conditions (https://onlinelibrary.wiley.com/terms-and-conditions) on Wiley Online Library for rules of use; OA articles are governed by the applicable Creative Commons License

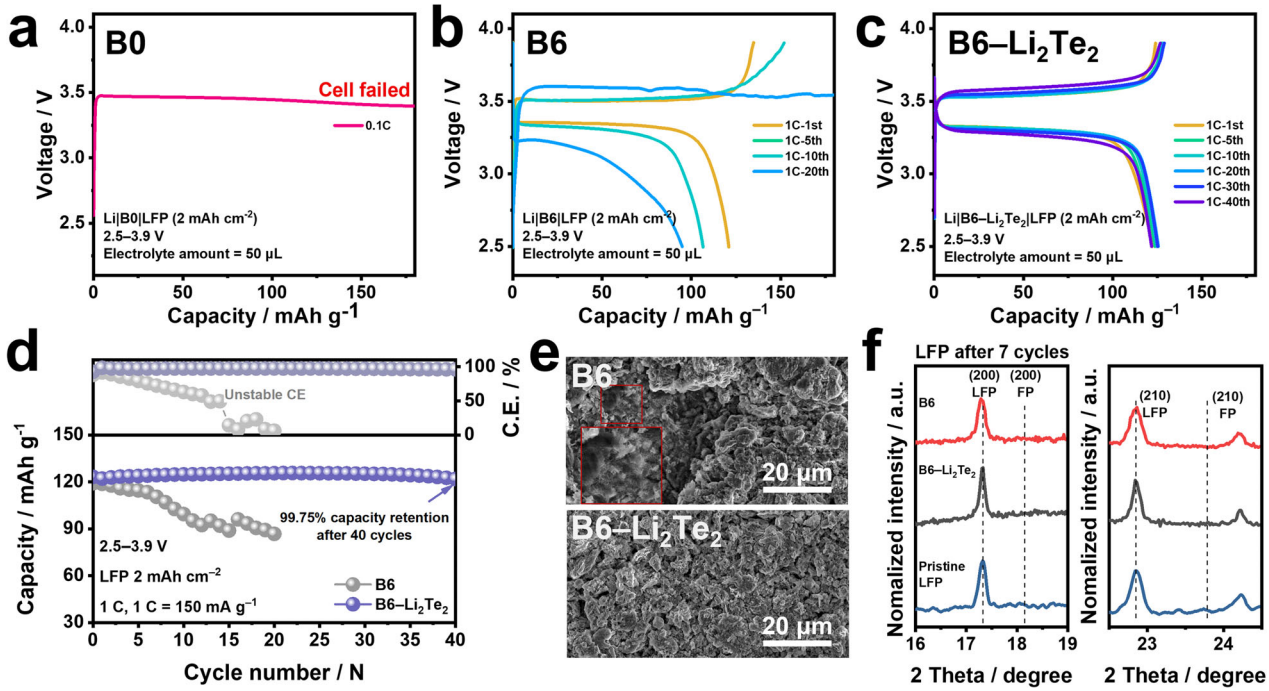


FIGURE 7 | Galvanostatic voltage profiles of Li||LFP full cells with (a) B0 at 0.1 C, (b) B6 at 1 C, and (c) B6–Li_2Te_2 at 1 C in the range of 2.5–3.9 V (vs. Li/Li^+) (1 C = 150 mA g^{-1}). (d) Evaluation of the long-term cycling performance in B6 and B6–Li_2Te_2 at 1 C, corresponding to (b,c), respectively. Post-mortem analysis was conducted at the seventh cycle to (d). (e) Comparison of the SEM images of the cycled Li-metal anode in B6 and B6–Li_2Te_2. Magnified SEM image of B6 indicating electrolyte decomposition consistent with Figure 5b. (f) XRD analysis of cycled LFP cathodes to investigate crystal structure preservation.

The Li-metal anode using different electrolytes exhibited distinct differences, as shown in Figure 7e. B6–Li_2Te_2 showed a smooth surface, while B6 exhibited a faded and damaged surface with large height differences in the stripping state.

The crystal structure changes of the LFP cathodes were analyzed using X-ray diffraction (XRD) [54]. The XRD patterns (Figure 7f) of the cycled LFP cathodes in B6 and B6–Li_2Te_2 revealed no crystal structural changes compared to the pristine LFP cathode with a typical orthorhombic phase [56]. To further validate the preservation of LFP crystal structure after cycling, we further fabricated and tested the re-fresh full cells using the cycled LFP cathodes with a fresh Li-metal anode and conventional carbonate electrolyte (1 M $LiPF_6$ dissolved in EC:DEC at a volume ratio 1:1 adding 5 wt.% FEC) (Figure S23). Interestingly, both re-fresh full cells using cycled LFP cathode in B6 and B6–Li_2Te_2 demonstrated almost identical electrochemical properties compared to the pristine LFP cathode. From these observations, it can be reasonably concluded that the significant difference in cycling performances of the full cells was contributed from the Li-metal anode rather than the cathode, and further highlighted the effectiveness of B6–Li_2Te_2 in high voltage Li-metal batteries even using DMSO solvent.

3 | Conclusion

In this work, Li_2Te was introduced into the SEI on the Li-metal anode surface as a quasi-decoupling component derived from the spontaneous reduction between Li-metal and Li_2Te_2 additive. This approach effectively protected the degradation of Li-metal anode by suppressing undesirable electrolyte decomposition even in highly reactive electrolytes such as high-DN DMSO-based electrolytes. Li_2Te was spontaneously formed through the reaction between Li and Li_2Te_2 on the Li-metal anode, thereby quasi-decoupling Li and the electrolyte. Li_2Te possessed three properties that improved the Li interface: (1) its near-zero interfacial electron transfer with DMSO, limiting the solvent reduction of DMSO; (2) its wide bandgap restricted bidirectional electron transfer, enabling quasi-decoupling between Li and DMSO; and (3) its high Li^+ conductivity facilitated Li^+ diffusion in the SEI layer that was comparable to Li_3N. Furthermore, the synergistic abilities in the lithiophilic nature of Li_2Te and Li_3N derived from $LiNO_3$ additive promoted the morphological regulation of electrodeposit Li-metal, effectively alleviating Li dendritic growth. As a proof-of-concept, we also proved the potential use of the proposed strategy in Li-metal batteries in a full cell coupling with the $LiFePO_4$ cathode. We believed that this new strategy, which quasi-decouples Li-metal from highly reactive solvents, offering valuable insight into electrolyte engineering toward stable Li-metal anodes for next-generation Li-metal batteries.

4 | Experimental Section

4.1 | Materials

DMSO (Sigma–Aldrich, 99.9%) was purified twice using 4 Å molecular sieves (beads 1.6–2.5 mm, Sigma–Aldrich) to remove residual moisture from the solvent. The sieves were dried at 180°C for 7 days under vacuum using a glass oven (B-585, Buchi). Li_2Te (Stanford Advanced Materials, 99.9%) was used

16163028, 2026, 48, Downloaded from https://advanced.onlinelibrary.wiley.com/doi/10.1002/adfm.75656 by Hanyang University Library, Wiley Online Library on [22/11/2026]. See the Terms and Conditions (https://onlinelibrary.wiley.com/terms-and-conditions) on Wiley Online Library for rules of use; OA articles are governed by the applicable Creative Commons License

as received, while LiTFSI (Solvionic, 99.9%), Te powder with 200 mesh (Sigma–Aldrich, 99.8%), and lithium nitrate ($LiNO_3$, Sigma–Aldrich, 99.999%) were dried to remove residual moisture at 110°C under vacuum for 3 days. The LFP (LFPO-21) powder for cathode materials was purchased from MTI Korea.

4.2 | Electrolyte Preparation

To reveal the functions of Li_2Te_2 and $LiNO_3$ as additives, nine electrolyte samples were prepared: (1) **B0**: 1 M LiTFSI in DMSO; (2) **B3**: 1 M LiTFSI in DMSO with 3 wt.% $LiNO_3$ as an additive; (3) **B6**: 1 M LiTFSI in DMSO with 6 wt.% $LiNO_3$ as an additive; (4) **B9**: 1 M LiTFSI in DMSO with 9 wt.% $LiNO_3$ as an additive; (5) **B6–Li_2Te_2**: 1 M LiTFSI and 0.05 M Li_2Te_2 in DMSO with 6 wt.% $LiNO_3$ as an additive; (6) **B6–0.1Li_2Te_2**: 1 M LiTFSI and 0.1 M Li_2Te_2 in DMSO with 6 wt.% $LiNO_3$ as an additive; (7) **B6–0.03Li_2Te_2**: 1 M LiTFSI and 0.03 M Li_2Te_2 in DMSO with 6 wt.% $LiNO_3$ as an additive; and (8) **0.05 M Li_2Te_2 in DMSO, PC** or **NMP**: 0.05 M Li_2Te_2 was dissolved in each solvent. In all instances, Li_2Te_2 was formed by adding Li_2Te and Te at a molar ratio of 1:1.

4.3 | Cathode Preparation

The LFP powder was applied as a cathode material. The cathode was fabricated by blending the active material (90 wt.%), Super P (2.5 wt.%), KS6 (2.5 wt.%), and polyvinylidene fluoride (5 wt.%) in NMP using a mixer (ARE-310, Thinky). The resulting uniform slurries were casted onto carbon-coated Al foil using a doctor blade and dried at 120°C for 2 h under vacuum to remove the remaining NMP and moisture. The electrode was pressed between stainless steel twin rollers at 80°C and punched into disks with a diameter of 10 mm, achieving an active material loading level of 13.3–13.5 mg cm^{-2} (approximately 2 mAh cm^{-2})

4.4 | Characterization

All the samples were prepared in an Ar-filled glove box (Mbraun, Unilab) below 0.1 ppm O_2 and H_2O. The densities and viscosities of the different electrolytes were investigated using an Anton Paar DMA 4500 M densitometer and an Anton Paar Lovis 2000 ME micro viscometer, respectively. Viscosity tests were conducted under various temperatures (30, 40, 50, and 60°C). UV–vis and Raman spectroscopies (laser wavelength: 532 nm; laser power: 45 mW; spectral resolution: 0.1 cm^{-1}) were conducted for electrolyte characterization. Optical images of 0.05 M Li_2Te and 0.05 M Li_2Te_2 in DMSO were obtained to visualize their color difference. The chemical components of the SEI layer corresponding to various electrolytes were analyzed using XPS (PHI Genesis, ULVAC PHI) and TOF-SIMS (TOF-SIMS 5, ION-TOF). The initial SEI layer and after on the Li-metal anode was investigated at the OCV state for 60 h by TOF-SIMS. A 100 × 100 μm^2 area was analyzed, and depth profiling was conducted over a 300 × 300 μm^2 area using a 2 keV of Cs^+ sputter beam for 1700 s. The same condition of TOF-SIMS analysis was applied to investigate the SEI layer after cycling. In addition, XPS analysis was performed on the samples after one cycle with a capacity loading and current density of 2 mAh cm^{-2} and 0.2 mA cm^{-2} and after five cycles with a capacity loading and current density of 0.5 mAh cm^{-2} and 0.5 mA cm^{-2}, respectively. The morphology of the Li-metal after deposition was investigated using SEM (Helios, FEI) and AFM (NX-10, Park Systems) at a capacity loading and current density of 2 mAh cm^{-2} and 0.2 mA cm^{-2}, respectively.

4.5 | Electrochemical Tests

Ionic conductivity was measured in the frequency range of 1 MHz to 1 mHz using a VMP-3e potentiostat (Bio-Logic) with a SUS||SUS symmetric cell using a 16π spacer. The ionic conductivity was calculated using the following equation [57, 58]:

$$\sigma = \frac{d}{RA} \tag{2}$$

where σ is the ionic conductivity (S cm^{-1}), R is the resistance measured by AC impedance (Ω), A is the electrode area (cm^2), and d is the thickness of the separator (cm).

The OCV cell was assembled using Li-metal (14 mm in diameter) and a Cu electrode (14 mm in diameter), separated by Whatman GF/C in CR2032 coin cells. The amount of electrolyte was 150 µL. The OCV tests were performed by monitoring the cell voltage for 60 h immediately after cell assembly. The AC impedance test was conducted from 1 MHz to 1 mHz using a VMP3 potentiostat (Bio-Logic) after five cycles at a capacity loading and current density of 0.5 mAh cm^{-2} and 0.5 mA cm^{-2}, respectively, in a Li||Li symmetrical cell configuration.

The average CE tests were performed using the as-prepared Li||Cu coin cells with 150 µL of different electrolytes to reveal the reversibility of the plated Li in the different electrolytes. The CEs were calculated using the following equation [50]:

$$CE_{avg} = \frac{nQ_C + Q_S}{nQ_C + Q_T} \tag{3}$$

In this study, a charge capacity (Q_T) of 3 mAh cm^{-2} was deposited onto the Cu foil at a current density of 0.5 mA cm^{-2}, and a charge capacity (Q_C) of 0.5 mAh cm^{-2} was used at a current density of 0.5 mA cm^{-2} during cycling. After 20 cycles (n), the final stripping capacity (Q_S) was measured to calculate the CE values. The nucleation potential was measured during the first plating step of the CE test at a capacity loading and current density of 3 mAh cm^{-2} and 0.5 mA cm^{-2}, respectively.

Galvanostatic tests using the Li||Li symmetrical cell configuration were conducted with Li-metal disks (14 mm in diameter) as both electrodes and Whatman GF/C as the separator. Two testing conditions were employed: (1) 50 µL with a capacity loading and current density of 2 mAh cm^{-2} and 2 mA cm^{-2}, respectively, and (2) 50 µL with a capacity loading of 4 mAh cm^{-2} and current density of 4 mA cm^{-2}. The full cell was assembled using Li-metal foil (16 mm in diameter) as the anode and LFP as the cathode, separated by Whatman GF/C in CR2032 coin cells. The amount of electrolyte was 50 µL, and the cells were operated within a voltage range of 2.5–3.9 V (versus Li/Li^+).

16163028, 2026, 48, Downloaded from https://advanced.onlinelibrary.wiley.com/doi/10.1002/adfm.75656 by Hanyang University Library, Wiley Online Library on [22/11/2026]. See the Terms and Conditions (https://onlinelibrary.wiley.com/terms-and-conditions) on Wiley Online Library for rules of use; OA articles are governed by the applicable Creative Commons License

4.6 | Postmortem Analysis

For postmortem analysis, cycled cells using B6 and B6–Li_2Te_2 were disassembled at a discharged state of 1 C after the seventh cycle, and each anode and cathode were analyzed using SEM (Helios, FEI) and XRD (D8 Advanced, Bruker), respectively. The cycled Li-metal anodes were observed at stripping state. The XRD analysis was conducted using an air-tight cell to prohibit air exposure. The recycled cells with the LFP cathode (10 mm in diameter) were assembled with a fresh Li-metal anode (14 mm in diameter) at 1 C using the electrolyte comprising 150 μL of 1 M $LiPF_6$ in EC:DEC (1:1 v/v) with 5 wt.% FEC (Dongwha Electrolyte).

4.7 | Theoretical Calculations

First-principles calculations were performed with the Vienna Ab-initio Simulation Package using the projector augmented-wave formalism and Perdew–Burke–Ernzerhofs exchange–correlation functional [59, 60]. Plane-wave cutoffs were set to 450 eV, and electronic self-consistency was converged to 1×10^{-5} eV. Moreover, ionic relaxations used −0.02 eV $Å^{-1}$ as the force convergence criterion. Bulk and slab k-point meshes were selected to yield a spacing of 0.02–0.03 $Å^{-1}$. These slabs included a ≥ 15 Å vacuum, and for asymmetric slabs, a dipole correction. Smearing was used for geometry relaxations, and the tetrahedron method with Blöchl corrections was used for DOS/PDOS. Employing the Henkelman group's Bader code, Bader charge analysis was used to quantify the interfacial charge transfer [61]. Surface energies of Li (001), Li_3N (001), and Li_2Te (001) slabs were calculated using DFT by comparing the total energies of relaxed slab models with their corresponding bulk phases, following $\gamma = (E_{slab} - N \cdot E_{bulk})/(2A)$, where A and n are the surface area and number of layers in the slab. Adsorption energies were computed as: $E_{ads} = E_{slab+Li} - E_{slab} - E_{Li}$. Migration barriers were calculated using the CI-NEB method, and molecular HOMO and LUMO energy levels were obtained from DFT calculations using the Gaussian 16 program [62]. The B3LYP and LANL2DZ basis sets were employed [63].

Acknowledgements

This work was supported by the National Research Foundation (NRF) of Korea grant funded by the Korean government (MSIT) (Nos. RS-2025-25441255 and RS-2025-00558312).

Conflicts of Interest

The authors declare no conflicts of interest.

Data Availability Statement

The data that supports the findings of this study are available in the supplementary material of this article.

References

1. H. Kim, J. Park, H. Kang, et al., "Synergetic Effects of Cation and Anion of $Mg(NO_3)_2$ as Electrolyte Additives in Stabilizing Li Metal Anode," *EES Batteries* 1, no. 3 (2025): 427–436, https://doi.org/10.1039/D5EB00025D.

2. Z. Xiao, X. Liu, F. Hai, et al., "Wide Temperature 500 Wh Kg^{-1} Lithium Metal Pouch Cells," *Angewandte Chemie International Edition* 64, no. 29 (2025): 202503693, https://doi.org/10.1002/anie.20250369.

3. Z. Li, Z. Chen, N. Sun, D. Wang, X. Yao, and Z. Peng, "Large Organic Polar Molecules Tailored Electrode Interfaces for Stable Lithium Metal Battery," *Angewandte Chemie International Edition* 19 (2024): 202400876, https://doi.org/10.1002/anie.202400876.

4. M. Rahman, U. Nisar, A. Abouimrane, I. Belharouak, and R. Amin, "Valuation of Anode Materials for High-Performance Lithium Batteries: From Graphite to Lithium Metal and Beyond," *Electrochemical Energy Reviews* 8 (2025): 14, https://doi.org/10.1007/s41918-025-00249-w.

5. Y. Xue, Y. Wang, H. Zhang, et al., "Molecular Design of Mono-Fluorinated Ether-Based Electrolyte for All-Climate Lithium-Ion Batteries and Lithium-Metal Batteries," *Angewandte Chemie* 137, no. 2 (2025): 202414201, https://doi.org/10.1002/ange.202414201.

6. J. Kim, D. G. Lee, J. H. Lee, et al., "Concurrent Electrode–Electrolyte Interfaces Engineering via Nano-Si_3N_4 Additive for High-Rate, High-Voltage Lithium Metal Batteries," *Energy & Environmental Science* 18, no. 7 (2025): 3148–3159, https://doi.org/10.1039/D4EE03862B.

7. Y. Jie, X. Liu, Z. Lei, et al., "Enabling High-Voltage Lithium Metal Batteries by Manipulating Solvation Structure in Ester Electrolyte," *Angewandte Chemie* 132, no. 9 (2020): 3533–3538, https://doi.org/10.1002/ange.201914250.

8. P. Zhou, Y. Xiang, and K. Liu, "Understanding and Applying the Donor Number of Electrolytes in Lithium Metal Batteries," *Energy & Environmental Science* 17, no. 21 (2024): 8057–8077, https://doi.org/10.1039/D4EE02989E.

9. S. Gu, Y. Zhang, M. Li, Q. Lin, G. Xu, and N. Zhang, "Internal Electron-Donation Allocation Design for Intrinsic Solubilization of Lithium Nitrate in Ester Electrolyte for Stable Lithium Metal Batteries," *Angewandte Chemie International Edition* 64, no. 1 (2025): 202410020, https://doi.org/10.1002/anie.202410020.

10. H. T. Duong, H. Van Ta, K. Van Tran, et al., "The Impact of DMSO Preservative on the Longevity of Commercial Level MnO_2@CNT || Zn Pouch Cells," *Materials Chemistry and Physics* 338 (2025): 130642, https://doi.org/10.1016/j.matchemphys.2025.130642.

11. M. S. Kim, Z. Zhang, J. Wang, et al., "Revealing the Multifunctions of Li_3N in the Suspension Electrolyte for Lithium Metal Batteries," *ACS Nano* 17, no. 3 (2023): 3168–3180, https://doi.org/10.1021/acsnano.2c12470.

12. H. M. Bintang, S. Lee, S. Shin, et al., "Stabilization Effect of Solid-Electrolyte Interphase by Electrolyte Engineering for Advanced Li-ion Batteries," *Chemical Engineering Journal* 424 (2021): 130524, https://doi.org/10.1016/j.cej.2021.130524.

13. H. Chen, K. Chen, L. Luo, et al., "LiNO 3 -Based Electrolytes via Electron-Donation Modulation for Sustainable Nonaqueous Lithium Rechargeable Batteries," *Angewandte Chemie International Edition* 63, no. 10 (2024): 202316966, https://doi.org/10.1002/anie.202316966.

14. J. Park, H. Kang, M. Agostini, et al., "Introduction of a Nitrate Anion With Solubility Mediator in a Carbonate-Based Electrolyte for a Stable Potassium Metal Anode," *Energy Storage Materials* 69 (2024): 103443, https://doi.org/10.1016/j.ensm.2024.103443.

15. W. Li, J. Chen, and T. Wang, "Electronic and Elastic Properties of Li_3N Under Different Pressure," *Physica B: Condensed Matter* 405, no. 1 (2010): 400–403, https://doi.org/10.1016/j.physb.2009.08.278.

16. Y.-H. Cao, Y.-F. Li, J.-W. He, et al., "Asymmetric Strain-Introduced Interface Effect on the Electronic and Optical Properties of the $CsPbI_3$/SnS van der Waals Heterostructure," *Advanced Materials Interfaces* 6, no. 24 (2019): 1901330, https://doi.org/10.1002/admi.201901330.

17. Y.-N. Wen and J.-M. Zhang, "Surface Energy Calculation of the Bcc Metals by Using the MAEAM," *Computational Materials Science* 42 (2008): 281–285, https://doi.org/10.1016/j.commatsci.2007.07.016.

16163028, 2026, 48, Downloaded from https://advanced.onlinelibrary.wiley.com/doi/10.1002/adfm.75656 by Hanyang University Library, Wiley Online Library on [22/11/2026]. See the Terms and Conditions (https://onlinelibrary.wiley.com/terms-and-conditions) on Wiley Online Library for rules of use; OA articles are governed by the applicable Creative Commons License

18. S. Kim, M. Aykol, and C. Wolverton, "Surface Phase Diagram and Stability of (001) and (111) $LiMn_2O_4$ Spinel Oxides," *Physical Review B* 92 (2015): 115411, https://doi.org/10.1103/PhysRevB.92.115411.

19. S. Alay-e-Abbas and A. Shaukat, "FP-LAPW Calculations of Structural, Electronic, and Optical Properties of Alkali Metal Tellurides: M_2Te [M: Li, Na, K and Rb]," *Journal of Materials Science* 46 (2011): 1027–1037, https://doi.org/10.1007/s10853-010-4868-7.

20. W. Li, J. Chen, and T. Wang, "Electronic and Elastic Properties of Li_3N Under Different Pressure," *Physica B: Condensed Matter* 405 (2010): 400–403, https://doi.org/10.1016/j.physb.2009.08.278.

21. R. Sun, S. Sun, X. Liang, et al., "Surface Charge Transfer Doping of MoS_2 Monolayer by Molecules With Aggregation-Induced Emission Effect," *Nanomaterials* 12, no. 1 (2022): 164, https://doi.org/10.3390/nano12010164.

22. H. Louis, T. E. Gber, F. C. Asogwa, et al., "Understanding the Lithiation Mechanisms of Pyrenetetrone-Based Carbonyl Compound as Cathode Material for Lithium-Ion Battery: Insight From First Principle Density Functional Theory," *Materials Chemistry and Physics* 278 (2022): 125518, https://doi.org/10.1016/j.matchemphys.2021.125518.

23. J. Yu, E. Baudrin, and A. A. Franco, "Diffusion Coefficient and Viscosity of Methyl Viologen Electrolyte Estimation Based on a Kinetic Monte Carlo Computational Approach Coupled With the Mean Square Displacement Method," *Batteries & Supercaps* 8, no. 3 (2024): 202400430, https://doi.org/10.1002/batt.202400430.

24. B. Han, Y. Zou, G. Xu, et al., "Additive Stabilization of SEI on Graphite Observed Using Cryo-Electron Microscopy," *Energy & Environmental Science* 14 (2021): 4882–4889, https://doi.org/10.1039/d1ee01678d.

25. J. Clay Hamill Jr, J. Schwartz, and Y.-L. Loo, "Influence of Solvent Coordination on Hybrid Organic–Inorganic Perovskite Formation," *ACS Energy Letters* 3, no. 1 (2018): 92–97, https://doi.org/10.1021/acsenergylett.7b01057.

26. N. Ding, S.-F. Chen, D.-S. Geng, et al., "Tellurium@Ordered Macroporous Carbon Composite and Free-Standing Tellurium Nanowire Mat as Cathode Materials for Rechargeable Lithium–Tellurium Batteries," *Advanced Energy Materials* 5 (2015): 1401999, https://doi.org/10.1002/aenm.201401999.

27. J. He, W. Lv, Y. Chen, et al., "Tellurium-Impregnated Porous Cobalt-Doped Carbon Polyhedra as Superior Cathodes for Lithium–Tellurium Batteries," *ACS Nano* 11, no. 8 (2017): 8144–8152, https://doi.org/10.1021/acsnano.7b03057.

28. H. Hao, Y. Liu, S. M. Greene, et al., "Tuned Reactivity at the Lithium Metal–Argyrodite Solid State Electrolyte Interphase," *Advanced Energy Materials* 13, no. 46 (2023): 2301338, https://doi.org/10.1002/aenm.202301338.

29. M. Mense, M. M. Bela, S. P. Kühn, et al., "ToF-SIMS Sputter Depth Profiling of Interphases and Coatings on Lithium Metal Surfaces," *Communications Chemistry* 8 (2025): 31, https://doi.org/10.1038/s42004-025-01426-0.

30. R. Li, X. Huang, H. Zhang, et al., "A Path towards High Lithium-Metal Electrode Coulombic Efficiency Based on Electrolyte Interaction Motif Descriptor," *Nature Communications* 16 (2025): 4672, https://doi.org/10.1038/s41467-025-59955-0.

31. S. Nanda, A. Bhargav, and A. Manthiram, "Anode-Free, Lean-Electrolyte Lithium-Sulfur Batteries Enabled by Tellurium-Stabilized Lithium Deposition," *Joule* 4, no. 5 (2020): 1121–1135, https://doi.org/10.1016/j.joule.2020.03.020.

32. Y. Choi, H. Kim, and J. Yoo, "Regulating the Polarization of Lithium Metal Anode via Active and Inactive 3D Conductive Mesh Structure," *Advanced Energy and Sustainability Research* 3, no. 10 (2022): 2200065, https://doi.org/10.1002/aesr.202200065.

33. M. Nagasaki, T. Masuda, K. Nishikawa, and K. Kanamura, "Surface State Change of Lithium Metal Anode in Full Cell during Long Term Cycles," *Electrochemistry* 87, no. 1 (2019): 84–88, https://doi.org/10.5796/electrochemistry.18-00080.

34. C. Liu, T. Li, H. Zhang, et al., "DMF Stabilized Li_3N Slurry for Manufacturing Self-Prelithiatable Lithium-Ion Capacitors," *Science Bulletin* 65 (2020): 434–442, https://doi.org/10.1016/j.scib.2019.11.014.

35. S. An, J. Li, Y. Sheng, C. Daniel, and D. Wood, "Long-Term Lithium-Ion Battery Performance Improvement via Ultraviolet Light Treatment of the Graphite Anode," *Journal of The Electrochemical Society* 163, no. 14 (2016): A2866–A2875, https://doi.org/10.1149/2.0171614jes.

36. F. Ding, W. Xu, X. Chen, et al., "Effects of Carbonate Solvents and Lithium Salts on Morphology and Coulombic Efficiency of Lithium Electrode," *Journal of The Electrochemical Society* 160, no. 10 (2013): A1894–A1901, https://doi.org/10.1149/2.100310jes.

37. M. Baek, J. Kim, K. Jeong, et al., "Naked Metallic Skin for Homo-Epitaxial Deposition in Lithium Metal Batteries," *Nature Communications* 14 (2023): 1296, https://doi.org/10.1038/s41467-023-36934-x.

38. S. Kim, K.-Y. Cho, J. Kwon, et al., "An Inorganic-Rich SEI Layer by the Catalyzed Reduction of $LiNO_3$ Enabled by Surface-Abundant Hydrogen Bonding for Stable Lithium Metal Batteries," *Small* 19, no. 26 (2023): 2207222, https://doi.org/10.1002/smll.202207222.

39. Q. Zhang, A. Yang, M. Wang, and W. Gao, "Thermally Enhanced SEI Chemistry via $LiNO_3$ Decomposition for High-Performance Lithium Metal Batteries," *Chemical Engineering Journal* 515 (2025): 163756, https://doi.org/10.1016/j.cej.2025.163756.

40. S. Heiskanen, J. Kim, and B. Lucht, "Generation and Evolution of the Solid Electrolyte Interphase of Lithium-Ion Batteries," *Joule* 3, no. 10 (2019): 2322–2333, https://doi.org/10.1016/j.joule.2019.08.018.

41. T. Takahashi, D. Wang, J. Hwang, and K. Matsumoto, "Intrinsic Effects of Electrolytes on Lithium Metal Deposition and Dissolution Investigated Through a Separator-Free Cell," *Energy Advances* 3, no. 7 (2024): 1653–1661, https://doi.org/10.1039/D4YA00245H.

42. Q. Peng, Z. Liu, L. Jiang, and Q. Wang, "Optimized Cycle and Safety Performance of Lithium–Metal Batteries With the Sustained-Release Effect of Nano $CaCO_3$," *Advanced Energy Materials* 12 (2022): 2104021, https://doi.org/10.1002/aenm.202104021.

43. Y. Xie, Y. Huang, Y. Zhang, et al., "Surface Modification Using Heptafluorobutyric Acid to Produce Highly Stable Li Metal Anodes," *Nature Communications* 14 (2023): 2883, https://doi.org/10.1038/s41467-023-38724-x.

44. Z. Wang, Y. Xia, T. Mao, et al., "Design Principles of $LiNO_3$ Inhibitor to Trigger Bilayer SEI and Wield Interface Reaction for Wide-Temperature-Range Lithium Metal Anodes," *Chemical Engineering Journal* 503 (2025): 158438, https://doi.org/10.1016/j.cej.2024.158438.

45. J. Park, Y. Jeong, M. H. Alfaruqi, et al., "Stable Solid Electrolyte Interphase for Long-Life Potassium Metal Batteries," *ACS Energy Letters* 7, no. 1 (2022): 401–409, https://doi.org/10.1021/acsenergylett.1c02354.

46. H. Kang, H. Park, J. Rizell, et al., "Regulation of Electrostatic Shielding Effect by 18-Crown-6 Ether for Achieving Stable Deposition of Potassium Metal Anodes," *ACS Energy Letters* 10 (2025): 2543–2552, https://doi.org/10.1021/acsenergylett.5c00797.

47. S. Ye, X. Chen, R. Zhang, et al., "Revisiting the Role of Physical Confinement and Chemical Regulation of 3D Hosts for Dendrite-Free Li Metal Anode," *Nano-Micro Letters* 14 (2022): 187, https://doi.org/10.1007/s40820-022-00932-3.

48. H. Shin, M. Baek, A. Gupta, K. Char, A. Manthiram, and J. Choi, "Recent Progress in High Donor Electrolytes for Lithium–Sulfur Batteries," *Advanced Energy Materials* 10, no. 27 (2020): 2001456, https://doi.org/10.1002/aenm.202001456.

49. Z. Li, R. Yu, S. Gui, H. Yang, and X. Guo, "A Pressure Responsive Artificial Interphase Layer of $BaTiO_3$ Against Dendrite Growth for Stable Lithium Metal Anodes," *Batteries & Supercaps* 5, no. 8 (2022): 202200142, https://doi.org/10.1002/batt.202200142.

50. B. Adams, J. Zheng, X. Ren, W. Xu, and J. Zhang, "Accurate Determination of Coulombic Efficiency for Lithium Metal Anodes and Lithium

16163028, 2026, 48, Downloaded from https://advanced.onlinelibrary.wiley.com/doi/10.1002/adfm.75656 by Hanyang University Library, Wiley Online Library on [22/11/2026]. See the Terms and Conditions (https://onlinelibrary.wiley.com/terms-and-conditions) on Wiley Online Library for rules of use; OA articles are governed by the applicable Creative Commons License

Metal Batteries," *Advanced Energy Materials* 8, no. 7 (2018): 1702097, https://doi.org/10.1002/aenm.201702097.

51. A. Mohammadi, L. Monconduit, L. Stievano, and R. Younesi, "Measuring the Nucleation Overpotential in Lithium Metal Batteries: Never Forget the Counter Electrode!," *Journal of The Electrochemical Society* 169, no. 7 (2022): 070509, https://doi.org/10.1149/1945-7111/ac7e73.

52. A. Pei, G. Zheng, F. Shi, Y. Li, and Y. Cui, "Nanoscale Nucleation and Growth of Electrodeposited Lithium Metal," *Nano Letters* 17 (2017): 1132–1139, https://doi.org/10.1021/acs.nanolett.6b04755.

53. K. Wen, L. Liu, S. Chen, and S. Zhang, "A Bidirectional Growth Mechanism for a Stable Lithium Anode by a Platinum Nanolayer Sputtered on a Polypropylene Separator," *RSC Advances* 8 (2018): 13034–13039, https://doi.org/10.1039/C8RA02140F.

54. R. Xu, C. Yan, Y. Xiao, M. Zhao, H. Yuan, and J. Huang, "The Reduction of Interfacial Transfer Barrier of Li Ions Enabled by Inorganics-Rich Solid-Electrolyte Interphase," *Energy Storage Materials* 28 (2020): 401–406, https://doi.org/10.1016/j.ensm.2019.12.020.

55. T. Pham and K. Lee, "Simultaneous Stabilization of the Solid/Cathode Electrolyte Interface in Lithium Metal Batteries by a New Weakly Solvating Electrolyte," *Small* 17 (2021): 2100133, https://doi.org/10.1002/smll.202100133.

56. M. Kassem and C. Delacourt, "Postmortem Analysis of Calendar-Aged Graphite/$LiFePO_4$ Cells," *Journal of Power Sources* 235 (2013): 159–171, https://doi.org/10.1016/j.jpowsour.2013.01.147.

57. H. Kim, "Controlling the Wettability Between Freestanding Electrode and Electrolyte for High Energy Density Lithium-Sulfur Batteries," *Journal of The Electrochemical Society* 165 (2018), A5006–A5013, https://doi.org/10.1149/2.0131801jes.

58. S. Park, J. Hwang, C. Yoon, H. Jung, and Y. Sun, "Stabilization of Lithium-Metal Batteries Based on the In Situ Formation of a Stable Solid Electrolyte Interphase Layer," *ACS Applied Materials & Interfaces* 10, no. 21 (2018): 17985–17993, https://doi.org/10.1021/acsami.8b04592.

59. G. Kresse and J. Furthmüller, "Efficient Iterative Schemes for Ab Initio Total-Energy Calculations Using a Plane-Wave Basis Set," *Physical Review B* 54 (1996): 11169–11186, https://doi.org/10.1103/PhysRevB.54.11169.

60. J. Perdew, K. Burke, and M. Ernzerhof, "Generalized Gradient Approximation Made Simple," *Physical Review Letters* 77, no. 18 (1996): 3865–3868, https://doi.org/10.1103/PhysRevLett.77.3865.

61. G. Henkelman, A. Arnaldsson, and H. Jónsson, "A Fast and Robust Algorithm for Bader Decomposition of Charge Density," *Computational Materials Science* 36 (2006): 354–360, https://doi.org/10.1016/j.commatsci.2005.04.010.

62. G. Henkelman, B. Uberuaga, and H. Jónsson, "A Climbing Image Nudged Elastic Band Method for Finding Saddle Points and Minimum Energy Paths," *The Journal of Chemical Physics* 113 (2000): 9901–9904, https://doi.org/10.1063/1.1329672.

63. J. irado-Rives and W. Jorgensen, "Performance of B3LYP Density Functional Methods for a Large Set of Organic Molecules," *Journal of Chemical Theory and Computation* 4 (2008): 297–306, https://doi.org/10.1021/ct700248k.

Supporting Information

Additional supporting information can be found online in the Supporting Information section.

Supporting File: adfm75656-sup-0001-SuppMat.docx.

16163028, 2026, 48, Downloaded from https://advanced.onlinelibrary.wiley.com/doi/10.1002/adfm.75656 by Hanyang University Library, Wiley Online Library on [22/11/2026]. See the Terms and Conditions (https://onlinelibrary.wiley.com/terms-and-conditions) on Wiley Online Library for rules of use; OA articles are governed by the applicable Creative Commons License